

Full paper



Enhancing electrochemical performance of thin film lithium ion battery via introducing tilted metal nanopillars as effective current collectors

Zhimin Qi^a, Jialiang Tang^b, Shikhar Misra^a, Cuncai Fan^a, Ping Lu^d, Jie Jian^a, Zihao He^e, Vilas G. Pol^b, Xinghang Zhang^{a,c}, Haiyan Wang^{a,e,*}

^a School of Materials Engineering, Purdue University, West Lafayette, IN, 47907, United States

^b Davidson School of Chemical Engineering, Purdue University, West Lafayette, IN, 47907, United States

^c School of Mechanical Engineering, Purdue University, West Lafayette, IN, 47907, United States

^d Sandia National Laboratories, Albuquerque, NM, 87185, United States

^e School of Electrical and Computer Engineering, Purdue University, West Lafayette, IN, 47907, United States

ARTICLE INFO

Keywords:

Li₂MnO₃

Au

Lithium ion battery

Oblique angle deposition

Nanocomposite

ABSTRACT

Novel Li₂MnO₃ (LMO)-Au nanocomposite thin film with tilted Au pillars has been synthesized by using an oblique angle deposition technique (OAD) in pulsed laser deposition. The tilt angle and dimension of the Au nanopillars can be tuned by varying the inclination angle of the incoming flux and the growth rate. The obtained LMO-Au nanocomposite structure exhibits an initial volumetric discharge capacity of 35.78 μAh cm⁻² μm⁻¹ for the 1st cycle but increases to 62.32 μAh cm⁻² μm⁻¹ at the 100th cycle. Such an increase in discharge capacity upon cycling is attributed to significantly increased reaction depth upon cycling, indicating that Au pillars function as effective current collectors and the LMO-Au interfaces improve the cycling stability. In addition, the LMO-Au nanocomposites display highly anisotropic optical complex dielectric function in-plane and out-of-plane, reduced bandgap, and high hardness of 10 GPa which almost doubled that of pure Li₂MnO₃. This study presents a novel approach for processing nanocomposite thin films with tunable tilted current collectors towards advanced thin film battery cathode, nanoscale plasmonic systems, and other oxide-metal hybrid electrochemical systems.

1. Introduction

Lithium ion batteries are one of the most promising energy storage methods in modern society, and significant research efforts have been focused on developing cathode materials with high electrochemical performance [1–4]. Li₂MnO₃ is a promising cathode material for high energy density applications due to its high theoretical capacity [5–7]. However, Li₂MnO₃ has a very low electrical conductivity (~10⁻⁹ S cm⁻¹) and it limits the power density of this cathode material. Most of the current attempts to improve the electrochemical performance are not satisfying [6–11]. The most commonly applied approach was to use carbon coating. For examples, Xiong et al. applied additional 10 wt% of carbon coating on the Li₂MnO₃ particles on top of 10 wt% of carbon black but it only delivered 52% capacity retention when the testing rate was increased from 0.09C to 3.40C [12]. Another approach is to integrate layered Li₂MnO₃ phase with spinel LiMn₂O₄ phase. He et al. utilized such integration approach, but the material only showed 45%

capacity retention from 0.1C to 10C [11]. Another common technique is to reduce particle dimensions. Vendra et al. synthesized Li₂MnO₃ nanowires with an average diameter of 50 nm and length of 1 μm and demonstrated superior rate performance [9]. Taminato et al. also demonstrated high capacity under high current densities with thin film Li₂MnO₃ at 12.6 nm [13]. Despite the apparent effectiveness of the approach, the small dimension could limit the energy density of the cathodes.

Nanocomposite materials contain multiphase building blocks with dimensions in nanometer range and exhibit improved physical properties. As a unique type of nanocomposites, vertically aligned nanocomposite (VAN) introduces vertical secondary phase domains in the matrix and presents a wide range of applications in tuning electrical transport properties [14–17], magnetic properties [15,18], and optical properties [19] due to the unique coexisting in-plane and out-of-plane strain and interface coupling. Furthermore, VAN is known to accommodate strain through vertically coupled domains [20–23]. Therefore,

* Corresponding author. School of Materials Engineering, Purdue University, West Lafayette, IN, 47907, United States.

E-mail address: hwang00@purdue.edu (H. Wang).

<https://doi.org/10.1016/j.nanoen.2019.104381>

Received 28 October 2019; Received in revised form 29 November 2019; Accepted 4 December 2019

Available online 7 December 2019

2211-2855/© 2019 Elsevier Ltd. All rights reserved.

VAN-based thin film electrodes could present great promise in achieving high conductivity and minimizing film delamination at film-to-substrate interfaces caused by volume change.

In this work, for the first time, a novel design of Au nanopillars incorporated into Li_2MnO_3 thin films through an Oblique Angle Deposition (OAD) method in pulsed laser deposition (PLD) has been achieved. PLD offers advantage in precise stoichiometry control of film composition which is ideal for complex oxides and high temperature ceramics [24]. The OAD technique is introduced in this work because a conventional co-growth of oxide-metal by PLD generally leads to metal particles in oxide matrix [17,19,24,26] with few cases growing as metal pillar in matrix [17,19,25,26]. OAD, on the other hand, introduces the shadowing effect by creating certain angle between the incoming source flux and the substrate, and the additional driving force can help achieve various film morphologies [27–30]. The schematic drawing of the OAD design in PLD is shown in Fig. 1b. Different from the previously reported particles-in-matrix design [17] (illustrated in Fig. 1a), the proposed Li_2MnO_3 -Au pillar configuration can provide more effective, continuous pathways for electrical and ionic transport across the entire cathode, and the more effective oxide-metal interfaces can provide mechanical integrity. Detailed microstructural analysis was conducted and assembled coin cell batteries using the unique Li_2MnO_3 -Au nanocomposite cathode were tested to explore the effects of the tilted Au nanopillars. Anisotropic optical properties originated from Au nanopillars were confirmed by optical measurement. Along with the nanoindentation experiments for exploring the mechanical integrity of the Li_2MnO_3 -Au nanocomposite cathodes, the work presents a promising approach for future incorporation of nanocomposite cathode designs for mechanically strong and high performance thin film batteries.

2. Results and discussion

2.1. Study of morphology and microstructure

Microstructural characterization of the Li_2MnO_3 -Au composite thin film was performed by X-ray diffraction (XRD), scanning electron microscopy (SEM), transmission electron microscopy (TEM), and high-angle annular dark-field scanning transmission electron microscopy (HAADF-STEM). The successful growth of the Au nanopillars is clearly demonstrated in the TEM/STEM images of Li_2MnO_3 -Au on the α - Al_2O_3 sample (Fig. 2). Specifically, Fig. 2a shows the low magnification TEM image of the sample. The Au nanopillars are clearly tilted 19° away from the out-of-plane direction and they are roughly 50 nm separated from

each other with the average diameter of ~ 6 nm as shown in Fig. 2a and a1. It is interesting to note that there are long nanopillars across the entire film thickness and short ones embedded in the film. The overall aspect ratio varies from 40 to 4, estimated from Fig. 2a. Fig. 2b shows the plan-view image of the sample, which further demonstrates the uniform distribution of Au nanopillars in-plane. Such tilted nanopillars are formed due to the OAD growth illustrated in Fig. 1. Due to the shadowing effects during OAD, the Au nanopillars are tilted 19° away from the incident angle. High resolution TEM image in Fig. 2a1 is presented to further illustrate the high quality epitaxial growth of such Au nanopillars in Li_2MnO_3 matrix. In cross-sectional STEM (Fig. 2d), Au-map (2d1) and Mn-map (2d2), there are some short Au nanorods near the film-substrate interface region suggesting the initial nucleation and seeding process of the Au nanopillars. In addition, there are some discontinuity between some of the nanopillars along the pillar growth direction. First, the small Au nanorods near the film-substrate interface are Au nucleates formed at the beginning stage of the growth but terminated to grow later due to shadowing effect [31]. Second, the discontinuity along nanopillar growth direction is due to the adatom diffusion. In general, OAD could introduce a large amount of porosity due to the limited adatom diffusion and shadowing effect, which commonly result in columnar-like morphology [32]. Several common types of morphologies formed with mixed sources are multilayered columns [33], zigzag-shaped multilayer columns [34], top/sides coated columns [35–37], tilted columns with porosity [38], and laterally assembled columns [39]. However, in this case, Li_2MnO_3 grows continuously as the matrix without obvious porosity while the Au grows as embedded tilted pillars. The Au adatoms could act as “adatoms diffusion facilitators” which facilitates the diffusion of Li_2MnO_3 adatoms, and therefore avoid formation of pores. Titled Au nanopillars form due to the tilted incoming flux and the resulted shadowing effects. The d -spacings along the out-of-plane direction are measured to be 4.731 Å and 2.285 Å, corresponding to $\text{Li}_2\text{MnO}_3(001)$ and Au(111). The epitaxial matching relationships of the Li_2MnO_3 -Au can be identified as $\text{Li}_2\text{MnO}_3(002)//\text{Au}(111)//\text{Al}_2\text{O}_3(0006)$ in the out-of-plane orientation and $\text{Li}_2\text{MnO}_3(131)//\text{Au}(\bar{1}\bar{1}1)//\text{Al}_2\text{O}_3(11\bar{2}3)$ for the in-plane orientation based on corresponding selected area diffraction pattern (SAED) taken from $\text{Al}_2\text{O}_3[10\bar{1}0]$ zone axis shown in Fig. 2c. The film composition is confirmed by energy dispersive spectroscopy (EDS) mapping in Fig. 2d, which confirmed the Au nanopillars in Li_2MnO_3 .

The XRD pattern in Fig. S1a indicates the highly textured growth of Li_2MnO_3 on both Al_2O_3 and Au-stainless steel (SS) substrates. The XRD

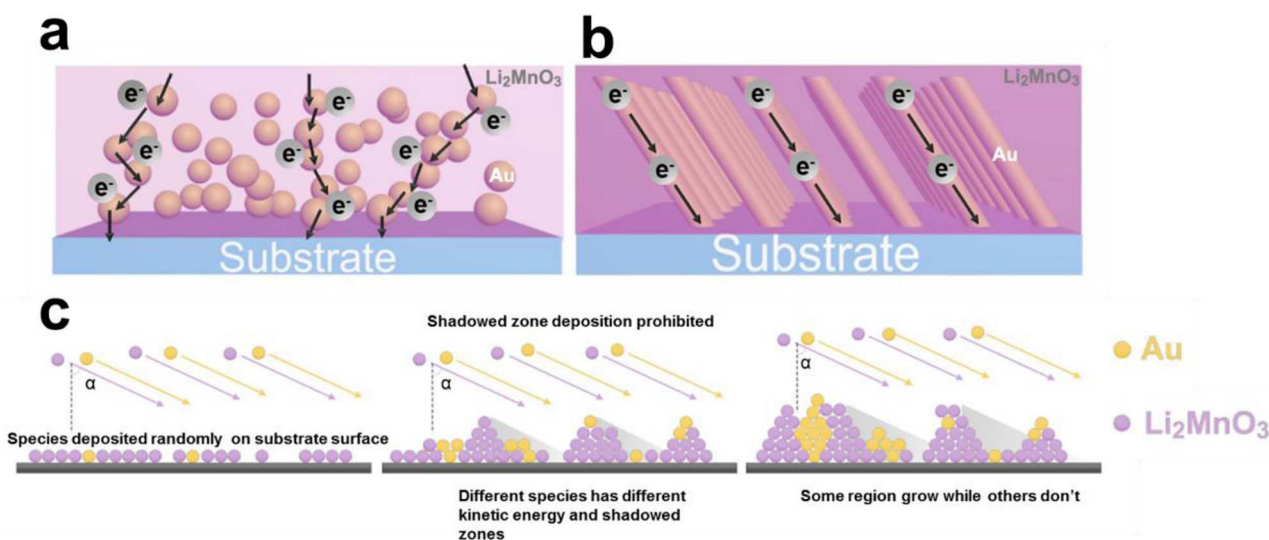


Fig. 1. The schematic drawing of comparison between a) Li_2MnO_3 -Au particle and b) Li_2MnO_3 -Au pillar composite structures; and illustration of c) expected growth mechanism.

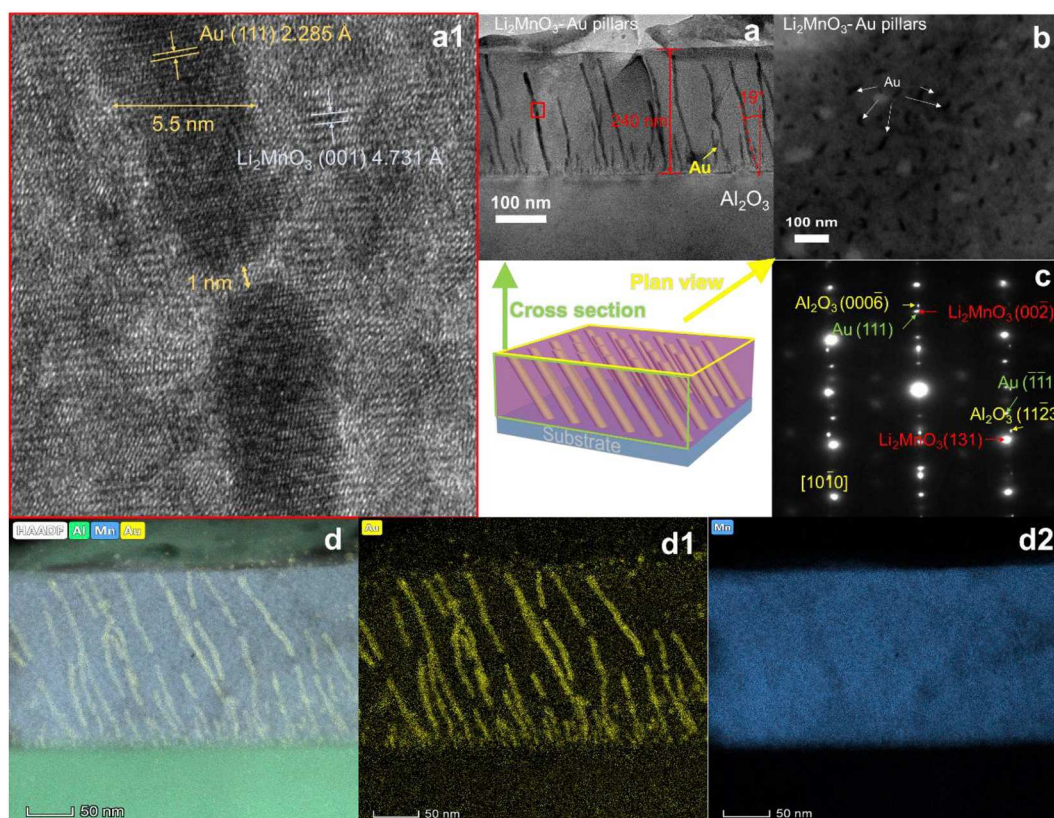


Fig. 2. a) Cross sectional TEM image of Li_2MnO_3 -Au composite on both Al_2O_3 substrate with a1) HRTEM shows the d spacing of Au (111) and Li_2MnO_3 (001); b) Plan-view TEM image indicates aligned Au pillars inside Li_2MnO_3 ; c) SAED pattern confirms the matching relationship between Au and Li_2MnO_3 matrix from the Al_2O_3 $[10\bar{1}0]$ zone axis; d), d1), d2) EDX mapping confirming the elemental distribution in the film.

shows the composite $\text{Li}_2\text{MnO}_3/\text{Au}$ has Li_2MnO_3 (001) d -spacing of 4.728 Å on Al_2O_3 and 4.762 Å on Au-SS, which is equal to a compressive strain of 0.14% and tensile strain 0.25% in c -axis direction compared to reported bulk value, respectively [40]. The different strain states could be from different substrates. Besides, the Li_2MnO_3 peaks have overall lower intensity on Au-SS than that on Al_2O_3 , which also matches our previous results [17]. As the Au existence in Al_2O_3 substrate was proved through TEM/STEM techniques, SEM images were taken for Li_2MnO_3 -Au on Au-SS substrate to prove the existence of Au. In Fig. S1b, the plan-view SEM image confirms the typical layered oxide growth morphology of Li_2MnO_3 with some embedded Au secondary phase, which are Au pillars based on the detailed information from both cross-sectional and plan-view images. We believe that the structural relationship of the sample on Au-SS substrate is very similar to that on Al_2O_3 substrate which is consistent with previous reports [17,41,42].

2.2. Cycling performance of Li_2MnO_3 -Au thin film cathode

The electrochemical performance of the Li_2MnO_3 -Au on Au-SS substrate has been evaluated in 2032R coin cells. The cycling behavior is better than thin film Li_2MnO_3 cathodes prepared by PLD and with thickness 6–20 times thicker than the reported work [13,43]. Fig. 3a shows the cycling performance of the thin film battery, and it shows a 35.78 $\mu\text{Ah cm}^{-2} \mu\text{m}^{-1}$ first cycle discharge capacity from constant current discharging step and total discharge capacity of 41.2 $\mu\text{Ah cm}^{-2} \mu\text{m}^{-1}$. It is worth noting that the cell exhibits 62.32 $\mu\text{Ah cm}^{-2} \mu\text{m}^{-1}$ constant current discharge capacity and 71.64 $\mu\text{Ah cm}^{-2} \mu\text{m}^{-1}$ total capacity at 100th cycle, which is roughly a 74% increase compared to the first cycle. This phenomenon was reported in literature as gradual phase transformation upon cycling [9]. However, the first cycle shows an unexpected large total charge capacity of 445.27 $\mu\text{Ah cm}^{-2} \mu\text{m}^{-1}$,

which can be translated to 1196.96 $\text{mAh}\cdot\text{g}^{-1}$ and it exceeds the theoretical capacity 459 $\text{mAh}\cdot\text{g}^{-1}$ for Li_2MnO_3 . Similar phenomenon was observed in pure Li_2MnO_3 , which is shown in Fig. S2a. However, this phenomenon is much more significant in pure Li_2MnO_3 and the cell failed at 10th cycle. This can be the proof of the increased film conductivity as the first overlarge charge capacity were also reported in other thin film work and were previously reported to be attributed to electrolyte decomposition [44,45].

Two plateaus can be observed in the 1st cycle charge curve but not in the 100th cycle charge curve. The plateau that appears around 3.75 V might be attributed to the diffusion limit of the lithium ions, representing the step which lithium ions overcome the energy barrier and be extracted from the cathode. It shows the slow activation nature for thin film batteries and only appears in the first charge cycle. Another plateau around 4.2 V can be from the electrolyte decomposition and the SEI formation because it gradually fades upon cycling. Besides, it is observed that the capacity increase starts from the 60th cycle. The cycle was performed after a cyclic voltammetry measurement at 59th cycle with sweep rate of 10 $\mu\text{V}/\text{s}$ as shown in Fig. 3b. This might be due to the deep reaction depth from the very slow scan rate, which can be converted to a very slow C-rate of 0.01C compared to the 0.5C of regular cycles. This can explain why the capacity starts fading after the 60th cycle but increased again at 80th cycle and continues to fade until the 100th cycle, as the deep cycle increased the depth of reaction and thus the amount of material that undergoes phase transformation. In addition, the extra capacity can be ascribed from the extended plateau around 3V, which is the lithium intercalation at 16c octahedral sites of the spinel phase, again, proves the abovementioned statement. It was previously reported that dislocation can form during cycling, which causes transport of trapped oxidized O^{2-} species to the surface and release O_2 [46]. Therefore, the improved cycling stability could be attributed to the

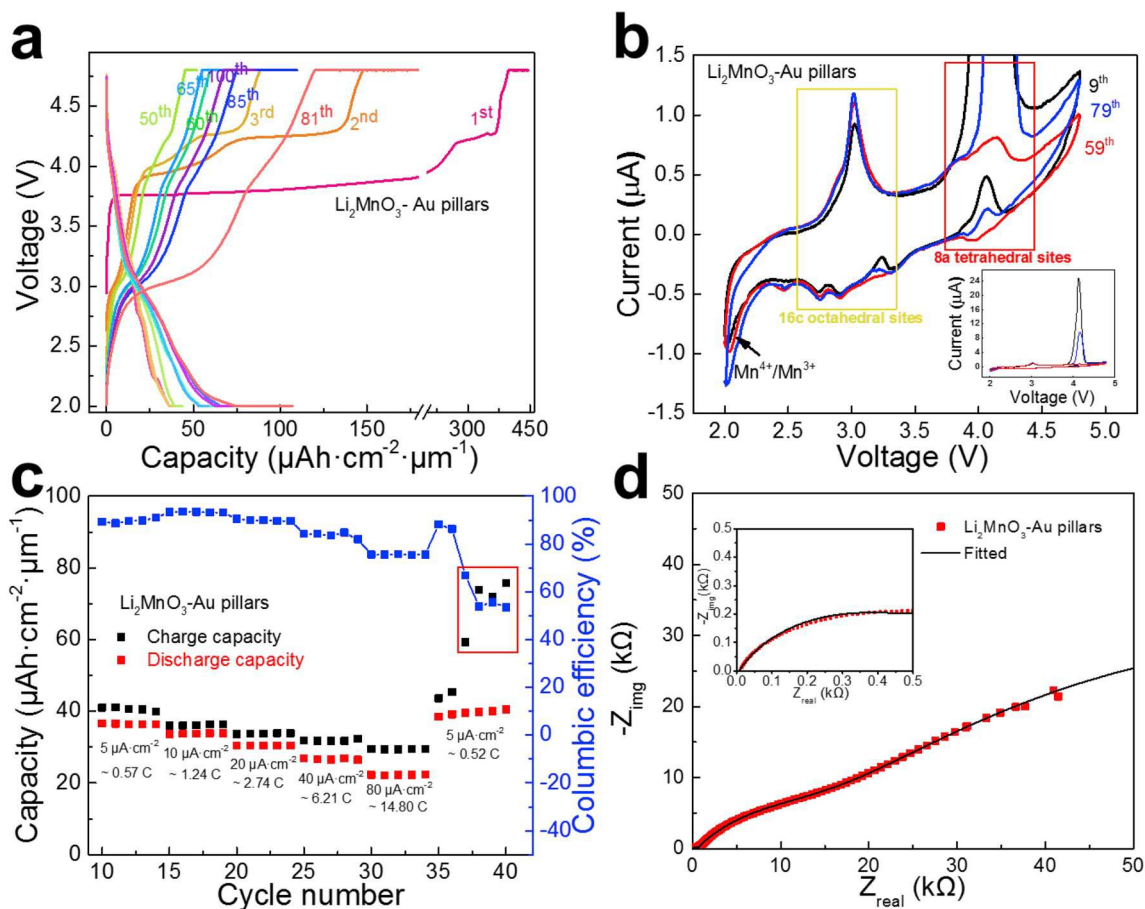


Fig. 3. a) Cycling performance of $\text{Li}_2\text{MnO}_3\text{-Au}$ after 100 cycles; b) Cyclic voltammograms of $\text{Li}_2\text{MnO}_3\text{-Au}$ with potential $20 \mu\text{V/s}$ sweep rate at 9th, 59th, and 79th cycles; c) C-rate performance test at current density of $5 \mu\text{A}/\text{cm}^2$, $10 \mu\text{A}/\text{cm}^2$, $20 \mu\text{A}/\text{cm}^2$, $40 \mu\text{A}/\text{cm}^2$, $80 \mu\text{A}/\text{cm}^2$ respectively with calculated columbic efficiency, and the corresponding estimated C-rate values are also labeled; d) EIS measurement of the cell after cycling.

$\text{Li}_2\text{MnO}_3\text{-Au}$ interfaces as it can act as defect sinks to absorb defects during cycling [47], which was not observed in the case of pure Li_2MnO_3 .

2.3. Reaction chemistry study by cyclic voltammetry measurement

Cyclic voltammetry (CV) measurement was conducted to study the redox reaction in the nanocomposite thin film electrode. Fig. 3b demonstrates the CV results at the 9th, 59th, and 79th cycle. The CV shows typical redox reactions of spinel type structure, where the redox pair around 3V is the lithium insertion in empty 16c octahedral sites and the peaks around 4V is that in empty 8a tetrahedral sites. Similar to the cycling test, the unexpected large anodic peak and the abnormal cathodic peak near 4.0 V confirms the existence of electrolyte decomposition. Similar behavior has been observed in pure Li_2MnO_3 , as shown in Fig. S2b, therefore the feature could be from the insulating nature of Li_2MnO_3 , especially in the dense thin film morphology [48]. However, while the pure Li_2MnO_3 failed after the 9th cycle, the $\text{Li}_2\text{MnO}_3\text{-Au}$ composite can be cycled for at least 100 cycles and the electrochemical performance increases upon cycling. It indicates that the Au pillars increase the conductivity of the overall composite film and the cathode will be gradually activated by cycles. The CV measurement at different sweep rates of $10 \mu\text{V/s}$, $20 \mu\text{V/s}$, $50 \mu\text{V/s}$, $75 \mu\text{V/s}$, $100 \mu\text{V/s}$, $200 \mu\text{V/s}$ is shown in Fig. S2c. There are two sets of redox reaction pairs appearing in the curves. The redox couples at $4.04\text{V}/3.95\text{V}$ and $3.04\text{V}/2.88\text{V}$ are the Li intercalation at 8a tetrahedral and 16c octahedral interstitial sites, respectively, and there are also some shoulder peaks next to the two main redox couples, which is typical in spinel type Mn-based materials

[49]. Furthermore, the oxidation peaks at 4.2 V are irrelevant to the sweep rates, which are the sign of electrolyte decomposition due to slow kinetics abovementioned, and the higher peak intensity at slower sweep rate suggests the slow reaction constant. However, the reaction is suppressed compared to pure Li_2MnO_3 , indicating the kinetics improvement from Au nanopillars. It is expected that such a dense structure could hinder the electrolyte penetration in the cathode and thus introducing porosity in the cathode could further improve the performance.

2.4. Rate performance and impedance analysis

The rate performance at the current density of $5 \mu\text{A}/\text{cm}^2$ to $80 \mu\text{A}/\text{cm}^2$ is shown in Fig. 3c, and the C-rate values are estimated and labeled at each corresponding current density. The $\text{Li}_2\text{MnO}_3\text{-Au}$ possesses excellent rate performance with 61% capacity retention at $80 \mu\text{A}/\text{cm}^2$ ($\sim 14.8\text{C}$) compared to $5 \mu\text{A}/\text{cm}^2$ ($\sim 0.57\text{C}$), which is higher than some of the previous reports [11,12]. The discharge capacity at 0.57C is of $36.45 \mu\text{Ah}/\text{cm}^2 \mu\text{m}^{-1}$ and the columbic efficiency is about 89.67%. Besides, the columbic efficiency doesn't decrease until the current density is at $40 \mu\text{A}/\text{cm}^2$, where the discharge capacity retains $\sim 73.15\%$ of its value at 0.57C . However, it is surprising that four cycles at the end of stepwise rate performance measurements show unexpectedly large charge capacity, and the charge-discharge curves of these four cycles are presented in Fig. S2d. It can be observed that the voltage first decreases then recovers during the charge process, which is not the diffusion limitation as discussed for the 1st cycle but instead the presence of side reaction [50]. This can be the potential explanation that the electrolyte decomposition peak around 4.2V disappears at the 59th cycle but shows

up in the 79th cycle, presented in Fig. 3b, as well as the reason that the 81st cycle experienced much significant increase regarding only charge capacity. Electrochemical Impedance Spectroscopy measurements of the cell at 100th cycle is presented in Fig. 3d. The model used to fit the spectrum contains three R-C circuits that can be possibly ascribed to cathode electrolyte interphase, charge transfer process in the cell, and the inhomogeneous Au/Li₂MnO₃ interfaces [51,52].

2.5. Anisotropic optical properties

Apart from the traditional electrochemical performance, optical anisotropy due to the tilted plasmonic Au nanopillars is expected and thus evaluated to study the tunable optical permittivity. Dielectric permittivity of the pure Li₂MnO₃ and Li₂MnO₃-Au samples are calculated by fitting the angular dependent ellipsometry data in the wavelength of 500 nm–1500 nm, and the results are presented in Fig. 4a–c. The ellipsometer parameter ψ and Δ was fitted with the use of general oscillator models to make it Kramers-Kronig consistent (see Methods section). The permittivity of Li₂MnO₃ (Fig. 4c) shows a normal dispersion curve that is characteristic of dielectric materials. Interestingly, the Li₂MnO₃-Au sample shows anisotropic permittivity in the in-plane and out-of-plane directions. The in-plane permittivity (ϵ'_{\parallel}) shows a typical dielectric behavior while the out-of-plane permittivity (ϵ'_{\perp}) shows the decrease in intensity indicating the existence of Au pillars in the out-of-plane direction. The anisotropic behavior of Li₂MnO₃-Au grants the potential of real-time online monitoring of battery charge-discharge behavior. The Au appears not just as pillars in the Li₂MnO₃ matrix but a certain degree of doping [26] in the Li₂MnO₃ lattice, as evidenced by the decrease of the bandgap for Li₂MnO₃-Au composite from 2.15 eV to 1.95 eV calculated using the Tauc plot in Fig. 4d. The measured transmittance plot and simulated curves by ellipsometry data are shown in Fig. S3, where the shape of the curves matches well.

2.6. Mechanical property measurement

Mechanical integrity of the cathodes is also critical for the long term performance of the battery [53,54]. The mechanical property of both pure Li₂MnO₃ and Li₂MnO₃-Au pillars was evaluated and compared by nano-indentation and the result is presented in Fig. S4a–b. It is seen that the hardness of Li₂MnO₃-Au has increased from averagely 4.7 GPa–10.7 GPa, which is about twice of pure Li₂MnO₃. The mean value increment can be attributed to the strengthening of interface between Li₂MnO₃ matrix and Au pillars. Note that the deviation parameter of Li₂MnO₃-Au is higher than that of pure Li₂MnO₃, which is presumably caused by structure nonuniformity.

2.7. Tunability of physical properties by tilting angle

It is interesting to note that the tilting angle can be effectively tuned by the PLD growth parameters as illustrated in Fig. 1. TEM samples of films grown at different tilt angles α were prepared, observed using HAADF technique and the result is shown in Fig. 5. The relationship between angles α and β is not fully understood and depends on both material properties and geometrical effects. The setup shown in Fig. 5a have target-to-substrate holder distance d_0 , actually target-to-substrate distance d' , and tilt angle α_1 . The composite film possesses thickness about 240 nm, long Au pillars with aspect ratio larger than 20, and pillar-substrate angle β_1 about 70°. Besides, it can be measured from the detailed view of individual pillar in Fig. S4e that the width is about 5.5 nm. On the other hand, the film exhibits thinner film (~180 nm) at a smaller tilt angle α_2 . Besides, the pillars are shorter yet wider (~11.1 nm) compared to the configuration in Fig. 5b, and the pillar-substrate angle β_2 is about 80°. Furthermore, the short pillars also hold different strain state compared to the long pillars. As mentioned, the long pillars experience a 0.14% compressive strain in Li₂MnO₃ along [001] direction

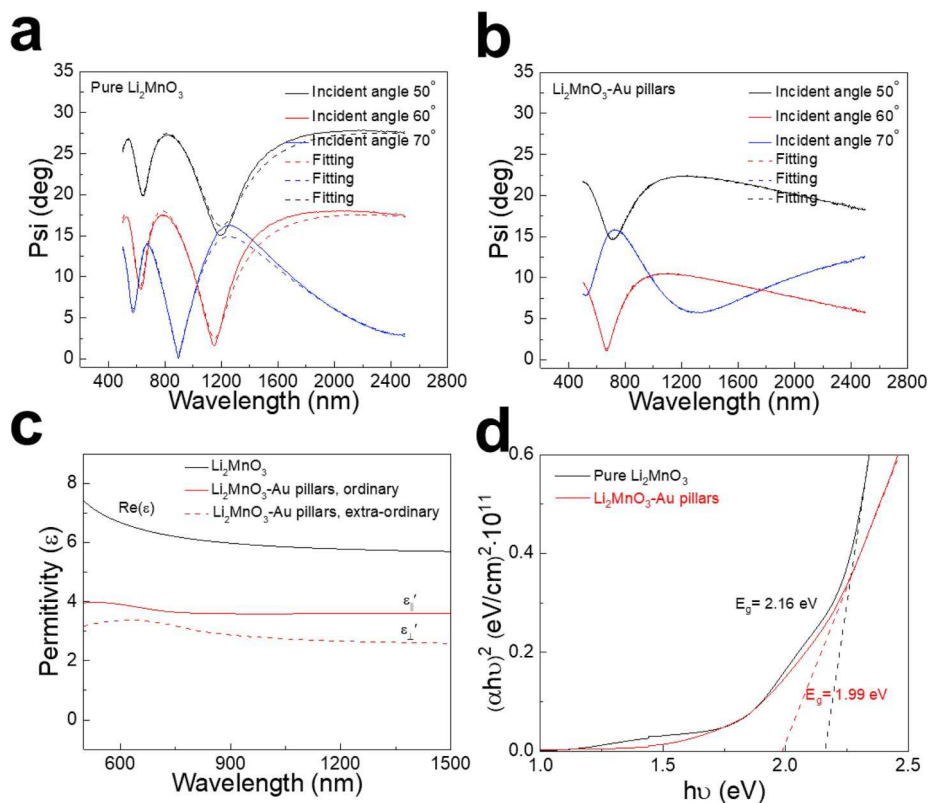


Fig. 4. Psi obtained by ellipsometer at 50°, 60° and 70° with fitted data of a) pure Li₂MnO₃ and b) Li₂MnO₃-Au pillars composite film; c) Permittivity data measured through ellipsometer indicating the increased absorption of Li₂MnO₃-Au and introduced anisotropy; d) Tauc plot obtained through transmission measurement deciding the bandgap of Li₂MnO₃ and Li₂MnO₃-Au pillar.

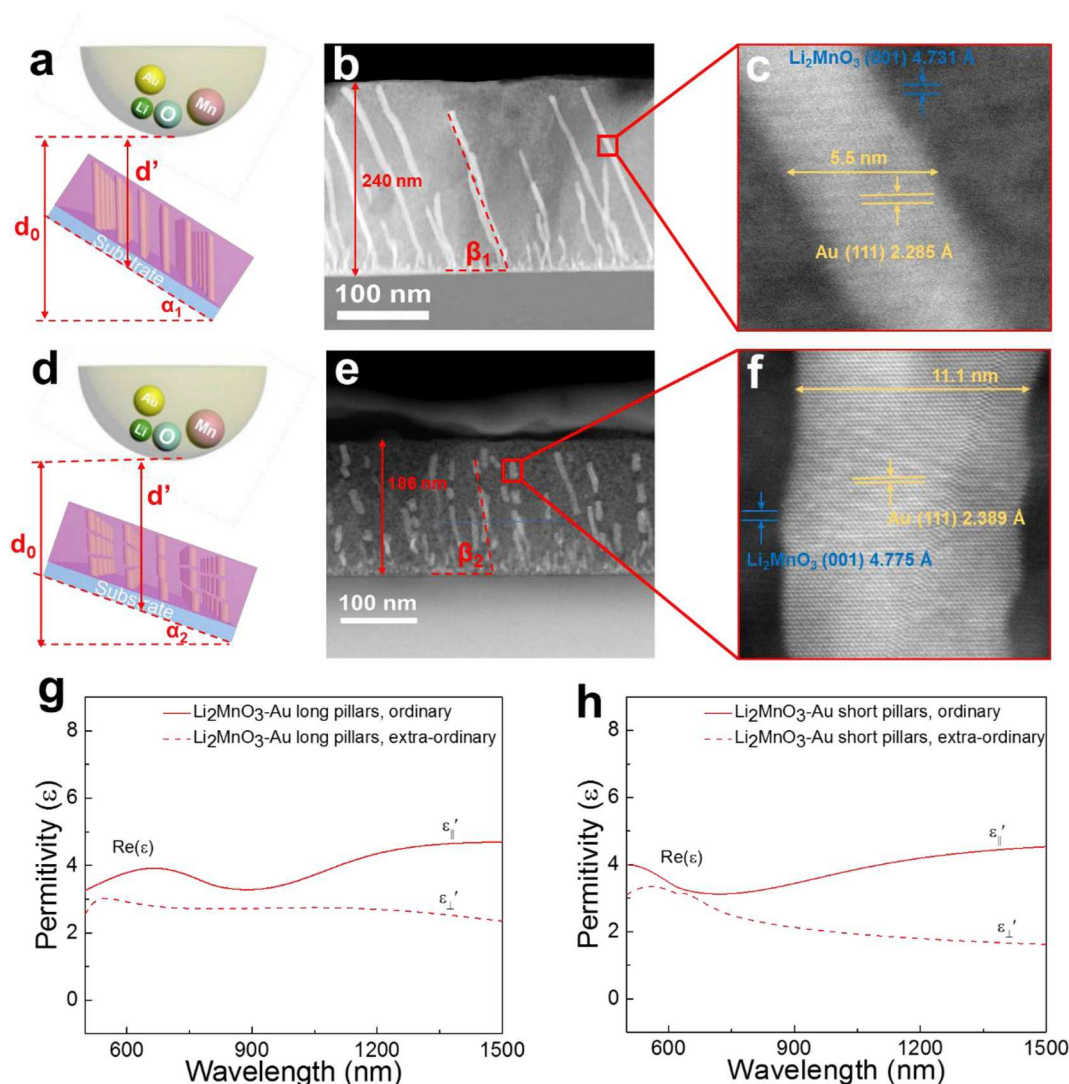


Fig. 5. a) Illustration of growth setup at higher tilt angle α_1 ; b) thin film grown with thicker film and smaller tilt angle β_1 ; c) HRSTEM showing Au pillar with small width; d) illustration of growth setup at higher tilt angle α_2 ; e) thin film grown with thinner film and larger tilt angle β_2 ; f) HRSTEM showing Au pillar with increased width. g) Permittivity curve of Li_2MnO_3 at higher tilt angle α_1 ; h) permittivity curve of Li_2MnO_3 at lower tilt angle α_2 .

and 2.77% compressive strain in Au along [111] direction, whereas the short pillars have 0.53% tensile strain of Li_2MnO_3 (001) and 1.66% tensile strain of Au (111). The reason that the smaller tilt angle renders this result can be explained by the growth rate controlled by the tilt angle. Smaller tilt angle indicates slower growth rate, further indicating increased stability of in-plane growth and suppression of out-of-plane growth [55]. This matches with the difference in thickness between the two configurations. It is known that smaller tilt angle α_2 result in less significant shadowing effect (more close to normal growth configuration). Therefore, the Li_2MnO_3 adatoms have higher chance to disrupt the continuous growth certain Au pillars, forming Au morphology that is more close to particle [27,55]. It is expected that the particle-in-matrix structure is less effective than pillar-in-matrix structure due to the inefficient conduction path and the detailed electrochemical performance study is still ongoing. Furthermore, the Au pillars of these two films demonstrate distinct optical behavior as observed in Fig. 5g and h. The permittivity (ϵ'_{\parallel}) along the in-plane direction presents a blue shift which might be due to the increased in-plane dimension of the Au pillars. Additionally, the out-of-plane permittivity (ϵ'_{\perp}) of shorter Au pillars decays faster than longer pillars due to its relatively higher volumetric percent.

3. Conclusion

Epitaxial Li_2MnO_3 -Au thin film cathodes are obtained using the oblique angle deposition method in pulsed laser deposition. The film morphologies such as film thickness, porosity, Au concentration, pillar tilt angle, pillar interspacing, pillar width and length can be effectively tuned by controlling the tilting angle and growth parameters. Such a unique nanopillars-in-matrix form presents the potential of creating even more complicated and novel structures by selecting the optimal materials combination, where new applications can be explored. The battery performance measured by cyclic voltammetry measurements, C-rate measurements, and impedance analysis all suggest the enhanced electrochemical performances due to the Au tilted nanopillars. Besides, the successful demonstration of angular tunability and correlation between thin film structure and optical properties suggests such opto-electrochemical systems can be engineered to achieve real-time battery performance monitoring and evaluation through optical approaches.

4. Experimental procedures

Composite film growth. Commercial Li_2MnO_3 powder from Pfaltz

& Bauer was mixed with 15% Li_2CO_3 (Alfa Aesar) to process the target. The Li_2MnO_3 target was sintered at 900 °C under oxygen flow for 24 h. The Li_2MnO_3 -Au composite target was prepared by attaching a piece of thin Au strip on central line of the Li_2MnO_3 target and the target was concentrically rotating during the deposition. The composite Li_2MnO_3 -Au film was deposited on both Al_2O_3 single crystalline substrates for structural analysis and stainless steel substrates buffered with Au (Au-SS) for electrochemical measurements. All depositions were conducted using pulsed laser deposition ($\lambda = 248$ nm, KrF source, Lambda Physik Compex Pro 205) at laser frequency of 10 Hz and energy of 2.5 J cm^{-2} . The target surface to substrate surface distance is kept at 5 cm. The temperature was set at 750 °C and oxygen partial pressure was maintained at 50 mTorr during deposition. Substrates were tilted at certain angle away from the substrate holder to achieve the oblique angle deposition configuration. The deposited film was cooled under 15 Torr O_2 at rate of 10 °C/min.

Structural characterization. X-ray diffraction pattern (XRD) was measured using a Cu $\text{K}\alpha 1$ ($\lambda = 1.5406 \text{ \AA}$) source (PANalytical Empyrean Diffractometer) to characterize the crystallinity of the samples. The measurement used 0.05° step size and 0.5 s step dwelling time with 2 theta angle ranging between 10° to 90° . Scanning electron microscopy (SEM, NovaNano SEM) was used to probe the surface morphology of composite film on Au-SS substrates. The acceleration voltage was set at 5 kV and spot size of 2.0 was used to be able to obtain high magnification images. Transmission electron microscopy (TEM), scanning transmission electron microscopy (STEM) (under high angle annular dark field, HAADF), and elemental distribution spectrum (EDS) were taken on sample deposited on Al_2O_3 using a FEI TALOS 200X system operated at 200 kV.

Coin cell battery assembly and electrochemical characterization. CR2032 coin cell was assembled in a glovebox filled with Ar (MBraun Labmaster, $\text{O}_2 < 0.1$ ppm, $\text{H}_2\text{O} < 0.1$ ppm) using Lithium metal disks (Sigma Aldrich) as anode, Celgard 2400 PP (Celgard) as separator, and 1 M LiPF_6 salt dissolved in 1:1 vol ratio EC:DEC (Sigma Aldrich) as electrolyte. The assembled coin cells were evaluated using a Arbin BTS2000 battery testing system. The cutoff voltage window was set between 2.0 V and 4.8 V as other reported literatures for better comparison [11,12]. Cycling performance was measured using a constant current/constant voltage program, which was cycled firstly under $5 \mu\text{A/cm}^2$ and constant voltage until the current decreased below $1 \mu\text{A}$. The Cyclic Voltammetry (CV) at different cycles were measured at $20 \mu\text{V/s}$, and CV at different voltage sweep rate ranging from $10 \mu\text{V/s}$ to $200 \mu\text{V/s}$ was also measured to evaluate the kinetics property of the battery. The rate performance measurement was conducted at current density respectively of $5 \mu\text{A/cm}^2$, $10 \mu\text{A/cm}^2$, $20 \mu\text{A/cm}^2$, and $80 \mu\text{A/cm}^2$, and the C-rate values of each current density were estimated using the actual discharge time. Electrochemical impedance spectrum was measured using Gamry Series G300 Potentiostat between 500 μHz and 200000 Hz at 4V at 100th cycle. The cell was aged at 4V constant voltage for 2 h to reach stable potential before the measurement started.

Optical characterization. A spectroscopic ellipsometry (JA Woolam RC2) was applied to evaluate the optical dielectric permittivity of all films was evaluated. The ellipsometer parameters ψ and Δ (\circ) were fitted using the CompleteEASE software with the mathematical relationship of $r_p/r_s = \tan(\psi)e^{i\Delta}$ where r_s and r_p are the reflection coefficient for the s-polarization and p-polarization light, respectively. The incident angles were 50° , 60° , and 70° . The ψ and Δ are measured at different angles to improve the accuracy of the fitted model. Li_2MnO_3 film was modeled using a Tauc-Lorentz oscillator and a Lorentz oscillator. Li_2MnO_3 -Au film was assumed to anisotropic since the Au pillar grows as a tilted pillar. Its in-plane permittivity was modeled using same as Li_2MnO_3 film while the out-of-plane permittivity was built using a Tauc-Lorentz oscillator and a Drude-Lorentz model.

Mechanical property measurement. Nanoindentation test was performed on a Hysitron TI 950 2000XYp with a Berkovich indenter. A loading-unloading function was applied to obtain force-displacement

curves, based on which the film hardness at various depths was measured using instrumented nanoindentation method [56].

Author contributions

HW conceived the project. ZQ designed and conducted the experiment and drafted the manuscript. JT assisted in electrochemistry and discussion of electrochemistry analysis under the supervision of VP. SM assisted in optical characterization and modeling under the supervision of HW. CF assisted in mechanical characterization under the supervision of XZ. PL and JJ performed HR-STEM. All authors contributed to the drafting of the manuscript.

Declaration of competing interest

The authors declare that they have no known competing financial interests or personal relationships that could have appeared to influence the work reported in this paper.

Acknowledgments

This work was supported by the U.S. Office of Naval Research (ONR, N00014-16-1-2465). The high-resolution TEM/STEM characterization at Purdue University was supported by the U.S. National Science Foundation (DMR-1809520).

Appendix A. Supplementary data

Supplementary data to this article can be found online at <https://doi.org/10.1016/j.nanoen.2019.104381>.

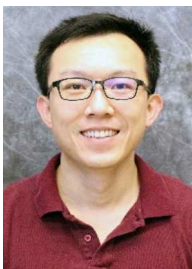
References

- [1] X. Zhang, A.-G. Porras-Gutierrez, A. Mauger, H. Groult, C. Julien, Nanotechnology of positive electrodes for Li-ion batteries, *Inorga* 5 (2017) 25, <https://doi.org/10.3390/inorganics5020025>.
- [2] N. Nitta, F. Wu, J.T. Lee, G. Yushin, Li-ion battery materials: present and future, *Mater. Today* 18 (2015) 252–264, <https://doi.org/10.1016/j.mattod.2014.10.040>.
- [3] R. Zhao, S. Zhang, J. Liu, J. Gu, A review of thermal performance improving methods of lithium ion battery: electrode modification and thermal management system, *J. Power Sources* 299 (2015) 557–577, <https://doi.org/10.1016/j.jpowsour.2015.09.001>.
- [4] C.M. Julien, A. Mauger, K. Zaghib, H. Groult, Comparative issues of cathode materials for Li-ion batteries, *Inorganic* 2 (2014) 132–154, <https://doi.org/10.3390/inorganics2020132>.
- [5] A.D. Robertson, P.G. Bruce, The origin of electrochemical activity in Li_2MnO_3 , *Chem. Commun. (J. Chem. Soc. Sect. D)* (2002), <https://doi.org/10.1021/cm030047u>, 2790–1.
- [6] S.H. Park, Y. Sato, J.K.K. Kim, Y.S. Lee, Powder property and electrochemical characterization of Li_2MnO_3 material, *Mater. Chem. Phys.* 102 (2007) 225–230, <https://doi.org/10.1016/j.matchemphys.2006.12.008>.
- [7] S.F. Amalraj, D. Sharon, M. Talianker, C.M. Julien, L. Burlaka, R. Lavi, et al., Study of the nanosized Li_2MnO_3 : electrochemical behavior, structure, magnetic properties, and vibrational modes, *Electrochim. Acta* 97 (2013) 259–270, <https://doi.org/10.1016/j.electacta.2013.03.029>.
- [8] R. Kataoka, N. Taguchi, T. Kojima, N. Takeichi, T. Kiyobayashi, Improving the oxygen redox stability of NaCl-type cation disordered Li_2MnO_3 in a composite structure of Li_2MnO_3 and spinel-type LiMn_2O_4 , *J. Mater. Chem.* 7 (2019) 5381–5390, <https://doi.org/10.1039/c8ta11807h>.
- [9] V.K. Vendra, T.Q. Nguyen, A.K. Thapa, J.B. Jasinski, M.K. Sunkara, Scalable synthesis and surface stabilization of Li_2MnO_3 NWs as high rate cathode materials for Li-ion batteries, *RSC Adv.* 5 (2015) 36906–36912, <https://doi.org/10.1039/C5RA01334H>.
- [10] M. Freire, O.I. Lebedev, A. Maignan, C. Jordy, V. Pralong, Nanostructured Li_2MnO_3 : a disordered rock salt type structure for high energy density Li ion batteries, *J. Mater. Chem.* 5 (2017) 21898–21902, <https://doi.org/10.1039/c7ta07476j>.
- [11] H. He, H. Cong, Y. Sun, L. Zan, Y. Zhang, Spinel-layered integrate structured nanorods with both high capacity and superior high-rate capability as cathode material for lithium-ion batteries, *Nano Res.* 10 (2017) 556–569, <https://doi.org/10.1007/s12274-016-1314-4>.
- [12] L. Xiong, M. Sun, Y. Xu, X. Du, X. Xiao, Synthesis of carbon coated Li_2MnO_3 cathode material with enhanced rate capability for lithium-ion batteries, *Solid State Ion.* 325 (2018) 170–175, <https://doi.org/10.1016/j.ssi.2018.08.008>.
- [13] S. Taminato, M. Hirayama, K. Suzuki, N.L. Yamada, M. Yonemura, J.Y. Son, et al., Highly reversible capacity at the surface of a lithium-rich manganese oxide: a

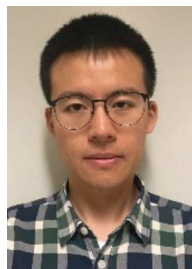
- model study using an epitaxial film system, *Chem. Commun.* 51 (2015) 1673–1676, <https://doi.org/10.1039/c4cc07758j>.
- [14] J. Huang, L. Li, X. Wang, Z. Qi, M.A.P. Sebastian, T.J. Haugan, et al., Enhanced flux pinning properties of YBCO thin films with various pinning landscapes, *IEEE Trans. Appl. Supercond.* 27 (2017), <https://doi.org/10.1109/TASC.2016.2637315>.
- [15] J. Huang, L. Li, P. Lu, Z. Qi, X. Sun, X. Zhang, et al., Self-assembled Co-BaZrO₃ nanocomposite thin films with ultra-fine vertically aligned Co nanopillars, *Nanoscale* 9 (2017) 7970–7976, <https://doi.org/10.1039/C7NR01122A>.
- [16] J. Jian, X. Wang, L. Li, M. Fan, W. Zhang, J. Huang, et al., Continuous tuning of phase transition temperature in VO₂ Thin films on c-cut sapphire substrates via strain variation, *ACS Appl. Mater. Interfaces* 9 (2017) 5319–5327, <https://doi.org/10.1021/acsmi.6b13217>.
- [17] Z. Qi, J. Jian, J. Huang, J. Tang, H. Wang, V.G. Pol, et al., LiNi_{0.5}Mn_{0.3}Co_{0.2}O₂/Au nanocomposite thin film cathode with enhanced electrochemical properties, *Nano Energy* 46 (2018) 290–296, <https://doi.org/10.1016/j.nanoen.2018.02.011>.
- [18] M. Fan, H. Wang, S. Misra, B. Zhang, Z. Qi, X. Sun, et al., Microstructure, magnetic, and magnetoresistance properties of La_{0.7}Sr_{0.3}MnO₃:CuO nanocomposite thin films, *ACS Appl. Mater. Interfaces* 10 (2018) 5779–5784, <https://doi.org/10.1021/acsmi.7b17398>.
- [19] J. Huang, T. Jin, S. Misra, H. Wang, Z. Qi, Y. Dai, et al., Tailorable optical response of Au-LiNbO₃ hybrid metamaterial thin films for optical waveguide applications, *Adv. Opt. Mater.* (2018) 1–9, <https://doi.org/10.1002/adom.201800510>, 1800510.
- [20] J. Huang, J.L. MacManus-Driscoll, H. Wang, New epitaxy paradigm in epitaxial self-assembled oxide vertically aligned nanocomposite thin films, *J. Mater. Res.* 32 (2017) 4054–4066, <https://doi.org/10.1557/jmr.2017.281>.
- [21] W. Zhang, A. Chen, Z. Bi, Q. Jia, J.L. Macmanus-Driscoll, H. Wang, Interfacial coupling in heteroepitaxial vertically aligned nanocomposite thin films: from lateral to vertical control, *Curr. Opin. Solid State Mater. Sci.* 18 (2014) 6–18, <https://doi.org/10.1016/j.cossms.2013.07.007>.
- [22] A. Chen, Z. Bi, Q. Jia, J.L. Macmanus-Driscoll, H. Wang, Microstructure, vertical strain control and tunable functionalities in self-assembled, vertically aligned nanocomposite thin films, *Acta Mater.* 61 (2013) 2783–2792, <https://doi.org/10.1016/j.actamat.2012.09.072>.
- [23] J.L. MacManus-Driscoll, P. Zerrer, H. Wang, H. Yang, J. Yoon, A. Fouchet, et al., Strain control and spontaneous phase ordering in vertical nanocomposite heteroepitaxial thin films, *Nat. Mater.* 7 (2008) 314–320, <https://doi.org/10.1038/nmat2124>.
- [24] M. Lambert, A. May, C.K. Akkan, N. Agarwal, O.C. Aktas, Ag-Al₂O₃ optical nanocomposites with narrow particle size distribution prepared by pulsed laser deposition, *Mater. Lett.* 137 (2014) 405–408, <https://doi.org/10.1016/j.matlet.2014.08.131>.
- [25] S. Misra, L. Li, D. Zhang, J. Jian, Z. Qi, M. Fan, et al., Self-assembled ordered three-phase Au–BaTiO₃–ZnO vertically aligned nanocomposites achieved by a templating method, *Adv. Mater.* 31 (2019) 1–8, <https://doi.org/10.1002/adma.201806529>.
- [26] J. Jian, X. Wang, S. Misra, X. Sun, Z. Qi, X. Gao, et al., Broad range tuning of phase transition property in VO₂ through metal-ceramic nanocomposite design, *Adv. Funct. Mater.* (2019) 1–12, <https://doi.org/10.1002/adfm.201903690>, 1903690.
- [27] A. Barranco, A. Borrás, A.R. González-Elipe, A. Palmero, Perspectives on oblique angle deposition of thin films: from fundamentals to devices, *Prog. Mater. Sci.* 76 (2016) 59–153, <https://doi.org/10.1016/j.pmatsci.2015.06.003>.
- [28] M. Suzuki, Practical applications of thin films nanostructured by shadowing growth, *J. Nanophotonics* 7 (2013), 073598, <https://doi.org/10.1117/1.JNP.7.073598>.
- [29] L. González-García, I. González-Valls, M. Lira-Cantu, A. Barranco, A.R. González-Elipe, Aligned TiO₂ nanocolumnar layers prepared by PVD-GLAD for transparent dye sensitized solar cells, *Energy Environ. Sci.* 4 (2011) 3426, <https://doi.org/10.1039/c0ee00489h>.
- [30] Y. Gaillard, V.J. Rico, E. Jimenez-Pique, A.R. González-Elipe, Nanoindentation of TiO₂ thin films with different microstructures, *J. Phys. D Appl. Phys.* 42 (2009), <https://doi.org/10.1088/0022-3727/42/14/145305>.
- [31] Y. He, J. Fu, Y. Zhao, Oblique angle deposition and its applications in plasmonics, *Front. Physiol.* 9 (2014) 47–59, <https://doi.org/10.1007/s11467-013-0357-1>.
- [32] Y. He, Y. Zhao, Advanced multi-component nanostructures designed by dynamic shadowing growth, *Nanoscale* 3 (2011) 2361–2375, <https://doi.org/10.1039/c1nr10103j>.
- [33] A.K. Kar, P. Morrow, X.T. Tang, T.C. Parker, H. Li, J.Y. Dai, et al., Epitaxial multilayered Co/Cu ferromagnetic nanocolumns grown by oblique angle deposition, *Nanotechnology* 18 (2007), <https://doi.org/10.1088/0957-4484/18/29/295702>.
- [34] L. González-García, G. Lozano, A. Barranco, H. Míguez, A.R. González-Elipe, TiO₂-SiO₂ one-dimensional photonic crystals of controlled porosity by glancing angle physical vapour deposition, *J. Mater. Chem.* 20 (2010) 6408–6412, <https://doi.org/10.1039/c0jm00680g>.
- [35] W. Smith, Y.P. Zhao, Superior photocatalytic performance by vertically aligned core-shell TiO₂/WO₃ nanorod arrays, *Catal. Commun.* 10 (2009) 1117–1121, <https://doi.org/10.1016/j.catcom.2009.01.010>.
- [36] Y. He, Y. Zhao, Improved hydrogen storage properties of a V decorated Mg nanoblade array, *Phys. Chem. Chem. Phys.* 11 (2009) 255–258, <https://doi.org/10.1039/b815924f>.
- [37] J.G. Fan, Y.P. Zhao, Gold-coated nanorod arrays as highly sensitive substrates for surface-enhanced Raman spectroscopy, *Langmuir* 24 (2008) 14172–14175, <https://doi.org/10.1021/la802248t>.
- [38] Y. He, Y. Zhao, J. Wu, The effect of Ti doping on the growth of Mg nanostructures by oblique angle codeposition, *Appl. Phys. Lett.* 92 (2008) 1–4, <https://doi.org/10.1063/1.2844852>.
- [39] C.M. Zhou, H.F. Li, D. Gall, Multi-component nanostructure design by atomic shadowing, *Thin Solid Films* 517 (2008) 1214–1218, <https://doi.org/10.1016/j.tsf.2008.05.049>.
- [40] T. Matsunaga, H. Komatsu, K. Shimoda, T. Minato, M. Yonemura, T. Kamiyama, et al., Dependence of structural defects in Li₂MnO₃ on synthesis temperature, *Chem. Mater.* 28 (2016) 4143–4150, <https://doi.org/10.1021/acs.chemmater.5b05041>.
- [41] C. Jacob, J. Jian, Y. Zhu, Q. Su, H. Wang, A new approach to investigate Li₂MnO₃ and Li(Ni_{0.5}Mn_{0.3}Co_{0.2})O₂ mixed phase cathode materials, *J. Mater. Chem.* 2 (2014) 2283–2289, <https://doi.org/10.1039/C3TA14413E>.
- [42] C. Jacob, J. Jian, Q. Su, S. Verkhoturov, R. Guillemette, H. Wang, Electrochemical and structural effects of in situ Li₂O extraction from Li₂MnO₃ for Li-ion batteries, *ACS Appl. Mater. Interfaces* 7 (2015) 2433–2438, <https://doi.org/10.1021/am5071305>.
- [43] K. Hikima, K. Suzuki, S. Taminato, M. Hirayama, S. Yasuno, R. Kanno, Thin film all-solid-state battery using Li₂MnO₃ epitaxial film electrode, *Chem. Lett.* 48 (2019) 192–195, <https://doi.org/10.1246/cl.180773>.
- [44] Y. Sugawara, S. Taminato, T. Hirayama, M. Hirayama, R. Kanno, Y. Ukyo, et al., Interfacial atomic structures of single-phase Li₂MnO₃ thin film with superior initial charge-discharge behavior, *J. Electrochem. Soc.* 165 (2018) A55–A60, <https://doi.org/10.1149/2.0261802jes>.
- [45] M. Hirayama, K. Suzuki, R. Kanno, S. Taminato, K. Hikima, S. Yasuno, Thin film all-solid-state battery using Li₂MnO₃ epitaxial film electrode, *Chem. Lett.* 48 (2019) 192–195, <https://doi.org/10.1246/cl.180773>.
- [46] Q. Li, Z. Yao, E. Lee, Y. Xu, M.M. Thackeray, C. Wolverton, et al., Dynamic imaging of crystalline defects in lithium-manganese oxide electrodes during electrochemical activation to high voltage, *Nat. Commun.* 10 (2019) 1–7, <https://doi.org/10.1038/s41467-019-09408-2>.
- [47] P. Liu, S. Zheng, K. Chen, X. Wang, B. Yan, P. Zhang, et al., Point defect sink strength of low-angle tilt grain boundaries: a phase field dislocation climb model, *Int. J. Plast.* 119 (2019) 188–199, <https://doi.org/10.1016/j.ijplas.2019.03.008>.
- [48] Z. Qi, J. Tang, J. Huang, D. Zemlyanov, V.G. Pol, H. Wang, Li₂MnO₃ thin films with tilted domain structure as cathode for Li-ion batteries, *ACS Appl. Energy Mater.* 2 (2019) 3461–3468, <https://doi.org/10.1021/acsaem.9b00259>.
- [49] R. Saroha, A. Gupta, A.K. Panwar, Electrochemical performances of Li-rich layered-layered Li₂MnO₃-LiMnO₂ solid solutions as cathode material for lithium-ion batteries, *J. Alloy. Comp.* 696 (2017) 580–589, <https://doi.org/10.1016/j.jallcom.2016.11.199>.
- [50] Y. Xie, Y. Jin, L. Xiang, Understanding Mn-based intercalation cathodes from thermodynamics and kinetics, *Crystals* 7 (2017) 1–22, <https://doi.org/10.3390/cryst7070221>.
- [51] Z. Wang, T. Zhao, J. Yao, Y. Kishikawa, M. Takei, Evaluation of the electrochemical characterizations of lithium-ion battery (LIB) slurry with 10-parameter electrical equivalent circuit (EEC), *J. Electrochem. Soc.* 164 (2017) A8–A17, <https://doi.org/10.1149/2.1421614jes>.
- [52] T. Osaka, D. Mukoyama, H. Nara, Review—development of diagnostic process for commercially available batteries, especially lithium ion battery, by electrochemical impedance spectroscopy, *J. Electrochem. Soc.* 162 (2015) A2529–A2537, <https://doi.org/10.1149/2.0141514jes>.
- [53] L. Lu, Y. Shen, X. Chen, L. Qian, K. Lu, Ultrahigh strength and high electrical conductivity in copper, *Science* 80 304 (2004) 422–426, <https://doi.org/10.1126/science.1092905>.
- [54] A. Benghalem, D.G. Morris, Microstructure and strength of wire-drawn Cu-Ag filamentary composites, *Acta Mater.* 45 (1997) 397–406, [https://doi.org/10.1016/S1359-6454\(96\)00152-8](https://doi.org/10.1016/S1359-6454(96)00152-8).
- [55] B.H. Stafford, M. Sieger, R. Ottolinger, A. Meledin, N.M. Strickland, S.C. Wimbush, et al., Tilted BaHfO₃ Nanorod Arti Fi Cial Pinning Centres in REBCO Fi Lms on Inclined Substrate Deposited-MgO Coated Conductor Templates 5th, 30, *Superconductor Science and Technology*, 2017, pp. 1–7.
- [56] W.C. Oliver, G.M. Pharr, An improved technique for determining hardness and elastic modulus using load and displacement sensing indentation experiments, *J. Mater. Res.* 7 (1992) 1564–1583.



Dr. Zhimin Qi received his Bachelor's degree from Zhejiang University of Technology in 2015 and his Ph.D. under the supervision of Prof. Haiyan Wang at Purdue University in 2019. His current research interest mainly focuses on the thin film lithium ion batteries.



Dr. Jialiang Tang received his Bachelor degree in Chemical Engineering from University of Texas at Austin, and his Ph.D from the Davidson School of Chemical Engineering at Purdue University. His research interest focuses on the study and development of high-capacity anode materials for Lithium and Sodium-ion batteries.



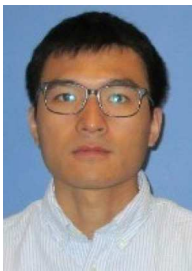
Zihao He received his Bachelor's degree from Shanghai Jiao-tong University in 2016 and master's degree from Carnegie Mellon University in 2018. He is currently a Ph.D. student in the department of Electrical and Computer Engineering at Purdue, under the supervision of Professor Haiyan Wang. His current research focuses on novel phase change materials with tunable transition properties.



Shikhar Misra is a fourth year PhD candidate in the MSE department at Purdue University advised by Prof. Haiyan Wang. In the past, he has interned at EPFL, University of Vienna and Hokkaido University. He graduated from Indian Institute of Technology (IIT) Kanpur with a Bachelors and Masters in Materials Science and Engineering. His research interests include developing new materials design through self-assembled metal-oxide and oxide nanocomposites epitaxial thin films for potential application as metamaterials and multiferroics.



Dr. Vilas Pol is Associate Professor at Purdue University's School of Chemical Engineering, USA. Pol has 17 years of research experience in the fields of materials chemistry, environmental- and electrochemical-engineering. He has authored/co-authored 140 research publications (h index 38), 4 book chapters and an inventor on 20 US patents/applications. He is a recipient of ACS Grand Prize, MRS science as art first prize, Intel prize, British Carbon Society's Brian Kelly award and a 'Gold Medal' in Sports. He won R and D 100 award (2015), AIChE's 'Sustainable Engineering Forum Research' Award (2016), and is a Fellow of World Technology Network.



Dr. Cuncai Fan received his Bachelor's degree from Wuhan University in 2012, and his Master's degree from Institute of Mechanics, Chinese Academy of Sciences in 2015. He joined Professor Xinghang Zhang's group in 2015 and completed his Ph.D. study at Purdue University in 2019. Currently (from 2019 Sep.), he is a postdoctoral research associate at Oak Ridge National Laboratory, with his research interests focused on the radiation damage effects in fusion nuclear materials.



Professor Xinghang Zhang, joined the School of Materials Engineering in Fall 2016. After his Ph.D. in 2001 from North Carolina State, he was a director-funded post-doc fellow at Los Alamos National Lab until joining Texas A & M University 2005. Professor Zhang's research interests are in nanostructured metallic systems (thin films and bulk); he couples materials processing with characterization and testing on a wide range of nanostructured metals in both ambient and harsh environments.



Dr. Ping Lu received his Bachelor's degree from Nanjing University (P. R. China) in 1984, and his Ph.D. from Arizona State University in 1989. He was a professor in New Mexico Institute of Mining and Technology from 1995 to 2008. He joined Sandia National Laboratories in 2008, and currently is a principal member of technical staff. His research interests include electronic thin-film deposition, microstructure, and structure-property relationship studies. He specializes in atomic-scale structural study of materials by utilizing transmission electron microscopy (TEM) as well as technical development of TEM and related techniques.



Professor Haiyan Wang is the Basil S. Turner Professor of Engineering with a joint appointment between the Schools of Materials Engineering and Electrical and Computer Engineering. Professor Wang's expertise is in electronic ceramic materials and covers processing and characterization of oxide- and nitride-based thin films in nanocomposite form for microelectronics, photonics, optoelectronics, ferroelectric and multiferroics, superconductors, solid oxide fuel cells, and batteries. She has published more than 490 journal papers (total citation over 16500, H-Factor 62), and is a Fellow of ASM International, ACerS, AAAS, APS and MRS.



Dr. Jie Jian received his bachelor's degree in Zhejiang University in 2011, and his Ph.D. degree from Texas A&M University in 2016, then he joined Professor Haiyan Wang's group in Purdue University as a post-doctoral fellow the same year. His research interests are electrical and optical properties of nanocomposite ceramic material, phase transition materials, and in situ TEM studies on mechanical, electrical and thermal properties of materials.